

# Correcting non-independent and non-identically distributed errors with surface codes

Konstantin Tiurev<sup>1</sup>, Peter-Jan H. S. Derk<sup>2</sup>, Joschka Roffe<sup>2</sup>, Jens Eisert<sup>2,3</sup>, and Jan-Michael Reiner<sup>1</sup>

<sup>1</sup>HQS Quantum Simulations GmbH, Haid-und-Neu-Strasse 7, 76131 Karlsruhe, Germany

<sup>2</sup>Dahlem Center for Complex Quantum Systems, Freie Universität Berlin, 14195 Berlin, Germany

<sup>3</sup>Helmholtz-Zentrum Berlin für Materialien und Energie, 14109 Berlin, Germany

A common approach to studying the performance of quantum error correcting codes is to assume independent and identically distributed single-qubit errors. However, realistic errors in experimental multi-qubit devices are typically neither independent nor identical across qubits. In this work, we develop and investigate the properties of topological surface codes tailored to a known noise channel by locally adapted Clifford conjugations. We show that the surface code locally tailored to non-uniform single-qubit noise in conjunction with a scalable matching decoder yields improved error thresholds and exponentially suppressed sub-threshold failure rates when compared to the Calderbank-Shor-Steane surface code. Furthermore, we study the behaviour of the tailored surface code under local two-qubit noise and show the role that code degeneracy plays in correcting such noise. The proposed methods do not require additional overhead in terms of the number of qubits and use a standard matching decoder, hence come at no extra cost compared to the standard surface-code error correction.

## 1 Introduction

Instances of topological *quantum error correcting codes* (QECCs) have shown tremendous success in providing a guideline towards realizing fault-tolerant logical qubits. Compared to other, more sophisticated prescriptions they are comparably experimentally viable due to the local structure of stabilizers and low-weight syndrome measurement operations. The most famous among these is the surface code, which only requires four-qubit parity measurements, admits fast and efficient decoding, and exhibits one of the highest thresholds among quantum codes with

Konstantin Tiurev: [konstantin.tiurev@gmail.com](mailto:konstantin.tiurev@gmail.com)

a two-dimensional qubit architecture.

The error threshold is usually defined for *independent and identically distributed* (iid) error models. By assuming that single-qubit Pauli errors occur independently with probability  $p$ , a logical qubit encoded in the surface code can be faithfully restored when  $p$  is below a threshold value  $p_{\text{th}} > 0$ . For a standard *Calderbank-Shor-Steane* (CSS) surface code in the presence of depolarizing noise and assuming error-free parity measurements, the error threshold is estimated to be around  $p_{\text{th}} \approx 16\%$  when a perfect-matching algorithm is used for decoding.

With the actual *experimental implementation* of large scale topological quantum error correcting codes moving closer to reality [1–5], interest is shifting towards devising physics non-agnostic schemes for quantum error correction that would respect physical desiderata that arise from properties of the chosen implementation. This reflects several aspects of the code design. In particular, the performance of an error correcting code will heavily depend on the *structure of noise* affecting the physical constituents. In order to accommodate this, steps have been taken recently to adapt quantum error correcting codes and decoding procedures to such kind of errors. As an example, biasing noise towards dephasing noticeably reduces the error threshold of the CSS surface code. Given some classical knowledge of structures that errors commonly take, the error correction procedure can be tailored to more efficiently handle such noise, resulting in dramatically reduced logical error rates and improved thresholds. As such, simply adapting the aspect ratio of the surface code allows to noticeably enhance the code performance [6]. References [7–11] employ a more involved procedure, referred to as Clifford deformation, to tailor the code stabilizers and a decoder to a given noise structure. The two prominent examples are the XY [9, 10, 12] and the XZZX [8, 13] codes, both significantly outperforming the CSS surface code for biased noise.

Tailoring an error correction strategy to a known noise structure hence plays a crucial role for protecting quantum information, and is expected to be increasingly important as technological development progresses.

In experimental reality, however, one must reasonably expect noise to obey a non-iid error statistics. Noise characteristics may, and in most cases actually do, notably vary from one qubit to another, which can compromise the performance of many error correcting schemes. Furthermore, errors can correlate across multiple qubits due to direct interactions [14, 15] or via coupling to a common bath [16]. However, despite the apparent practical importance, the performance and optimization of QECCs in the presence of non-iid noise have been barely investigated. Several works have discussed correction of multi-qubit correlated errors [16–21], while, to the best of our knowledge, effect of non-identically distributed errors has only been studied in Refs. [22, 23].

In this work, we investigate the error correcting capabilities of the surface code in the presence of non-iid noise and propose ways to adapt the error correction procedure to more efficiently battle such noise. Firstly, we design a Clifford-deformed version of the surface code tailored to correct *non-identically distributed Pauli errors* with a matching decoder. We numerically benchmark the performance of the noise-tailored code versus non-optimized surface codes and demonstrate (i) exponential suppression of the sub-threshold logical error rates as a function of the code distance and (ii) an improved error threshold. Secondly, we show that similar improvements in error correcting capabilities of the surface code can be achieved by modifying input parameters of a matching decoder in a situation where qubits experience *non-identically distributed total error rates*. Finally, we study the behaviour of the surface code under a combination of single-qubit and local two-qubit errors. We show that the code stabilizers can be adapted to a known correlated noise structure to make syndrome configurations plausible for efficient perfect-matching decoding. Strikingly, our numerical simulations suggest that the sub-threshold scaling can be significantly improved even when no information about the noise structure is provided to the decoder. Instead, it suffices to merely account for code degeneracy, which is determined by a combination of a surface code geometry and a noise model. We expect this framework to be useful when tailoring codes to physical needs that arise in superconducting, cold

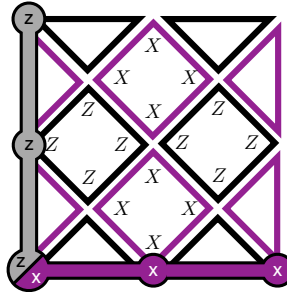


Fig. 1: The CSS surface code. Star and plaque stabilizers are defined in Eq. (1) and shown with black and purple tiles, respectively. Logical  $\bar{X}$  ( $\bar{Z}$ ) operators are chains of single-qubit Pauli operators shown in purple (grey).

atomic, trapped ion, or photonic architectures.

The remainder of this article is organized as follows. Section 2 introduces the standard surface code and a decoding algorithm based on *minimum weight perfect matching* (MWPM) and shows that the code can be locally transformed by a process known as Clifford deformation. Section 3 introduces a variant of the surface code designed to correct non-identically distributed Pauli errors. In Sec. 4, we study the performance of the surface code under correlated errors between nearest-neighbor data qubits and point out a crucial role of code degeneracy [24] for correcting such errors. We conclude in Sec. 5 by discussing potential directions for improving the performance of noise-tailored error correcting codes.

## 2 Overview of the surface code

In order to appreciate the idea of tailoring the code design to a given noise, we start by reviewing elements of the surface code. The basic idea of a QECC is to redundantly encode the state of a single logical qubit into a larger array of noisy physical qubits. Encoding is achieved by fixing  $N - 1$  independent parity check operators, or stabilizers, on  $N$  bare qubits, with the remaining degrees of freedom corresponding to the logical qubit. Throughout the course of computation, errors are detected by measuring stabilizers and subsequently corrected. If bare qubit errors are sufficiently rare, i.e., occur with probability below the threshold value  $p_{\text{th}}$ , quantum information can be faithfully restored. The challenge is to design practical QECCs that allow to uniquely detect and correct the most common errors in realistic experimental settings. Among other choices, the surface code offers particularly high thresholds while requiring only parity checks within sets of nearest-neighbor qubits in a two-dimensional qubit layout. Below we describe the basic operation of the surface code and the decoding procedure.

## 2.1 CSS surface code

The surface code of distance  $d$  is a stabilizer quantum error correcting code of  $N = d_1 d_2 + (d_1 - 1)(d_2 - 1)$  qubits arranged on the edges on a rectangular lattice  $L$  of  $d_1 \times d_2$  vertices with  $d = \min(d_1, d_2)$ . The code space of the surface code is described by its stabilizer group  $\mathcal{S}$ , which is an Abelian subgroup of the  $N$ -qubit *Pauli group*  $\mathcal{P}_N$ , the group generated by products of single-qubit Pauli operators together with suitable scalar factors. Particularly, the stabilizer group of the standard surface code is generated by two types of stabilizers, namely, *star* and *plaquette* operators defined as

$$A_{\diamond} := \prod_{i \in \diamond} X_i \quad \text{and} \quad B_{\square} := \prod_{j \in \square} Z_j, \quad (1)$$

respectively. Here and in the following,  $X_i$ ,  $Y_i$  and  $Z_i$  denote the respective qubit Pauli operators applied to qubit with vertex label  $i \in L$ . We will also use  $X$ ,  $Y$ ,  $Z$  for the abstract Pauli operators when the support is not specified.  $\diamond$  and  $\square$  denote cells as subsets of  $L$  of four nearest-neighbor qubits and form, respectively, dual and primal sub-lattices illustrated in Fig. 1. Operators on the logical qubit are defined as chains of single-qubit Pauli operators connecting opposite edges of the lattice and commuting with all stabilizers. Measuring stabilizers hence does not reveal information about the state of the logical qubit. With the above definition (1), a logical  $\bar{X}$  ( $\bar{Z}$ ) operator corresponds to any chain of single-qubit  $X$  ( $Z$ ) operators connecting left and right (top and bottom) edges of the lattice in Fig. 1. Basis state vectors of the logical qubit are then defined in a standard way,

$$\bar{Z}|0\rangle_L = (+1)|0\rangle_L, \quad \bar{Z}|1\rangle_L = (-1)|1\rangle_L \quad (2)$$

and, by construction, obey

$$\bar{X}|0\rangle_L = |1\rangle_L, \quad \bar{X}|1\rangle_L = |0\rangle_L. \quad (3)$$

Stabilizers (1) are measured throughout the computation and the result of their measurement, also called the error syndrome, indicates which error has occurred. We note that stabilizer measurement is itself a process prone to errors and the measurement apparatus can in principle return incorrect eigenvalues. In such a case, repetitive extraction of syndromes is necessary to define the correct syndrome configuration. Here we restrict our analysis to a simpler case of perfect syndrome measurements and only consider errors that occur in data qubits.

For the CSS surface code defined according to Eq. (1), a single-qubit  $X$  ( $Z$ ) error commutes with

all star (plaquette) stabilizers and therefore only creates pairs of defects, or anyons, in the primal (dual) sub-lattice. Decoding is performed by finding the most probable chains of errors corresponding to a measured syndrome. The most commonly used decoder is based on the MWPM algorithm. It first constructs an input graph by assigning each measured defect a vertex, with weighted edges corresponding to chains of errors connecting two defects. Assuming that single-qubit  $X$  and  $Z$  errors occur with equal probability  $p$ , weights  $w_{i,j} \geq 0$  between vertices  $i, j \in L$  are chosen according to

$$w_{i,j} := -\log P_{i,j}, \quad (4)$$

where

$$P_{i,j} := p^{l_x + l_z} \quad (5)$$

is the probability of connecting two stabilizers that have horizontal distance  $l_x$  and vertical distance  $l_z$  by the shortest chain of single-qubit errors. Substituting Eq. (5) into Eq. (4) and ignoring a common coefficient  $-\log(p) > 0$ , the edges of the input graph are weighted according to the *Manhattan distance*

$$w_{i,j} = l_x + l_z, \quad (6)$$

which is the distance induced by the vector  $l_1$ -norm.

The algorithm then searches for a perfect matching such that the sum of the weights of the edges is minimal, corresponding to a maximally probable error chain, and returns indices of defects that should be locally paired by the correction. MWPM in its standard implementation assumes single-qubit  $X$  and  $Z$  errors independently, hence decoding takes place separately in primal and dual sub-lattices. Pauli- $Y$  errors, however, create pairs of defects in the two sub-lattices simultaneously, which compromises the capabilities of the standard matching decoder.

We note that more involved decoding algorithms can take correlations beyond the paradigm of independent  $X$  and  $Z$  errors into account and therefore demonstrate the improved decoding efficiency in the presence of  $Y$  errors. Such decoders are, however, based on more computationally heavy algorithms or require extensive pre-processing, presumably rendering them incompatible with fast on-the-go error correction in real quantum hardware. Hence, here we will focus exclusively on the matching algorithm and its variations.

## 2.2 Clifford-deformed surface codes

In the previous section, we have constructed a CSS surface code according to the stabilizers of Eq. (1).

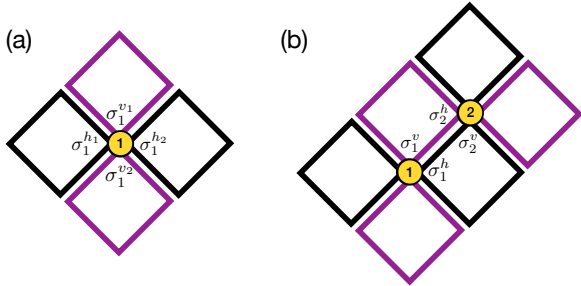


Fig. 2: Stabilizers of the surface code surrounding (a) a single qubit and (b) two qubits.  $\sigma_i^s$  denotes a Pauli operator measured on qubit  $i \in L$  (yellow circle) by stabilizer  $s$ .

One can, however, equivalently choose an alternative set of stabilizers by applying single-qubit Clifford transformations to the stabilizers of the CSS code. Building on the steps taken in Ref. [7] we refer to any code derived in such a way as a Clifford-deformed QECC.

In a Clifford-deformed surface code, quantum states of each of the physical qubits  $i \in L$  of the code are conjugated with a unitary  $U \in C_1/U(1)$  from the single-qubit *Clifford group* of order 24. The Clifford group is the group of unitaries that maps Pauli operators onto Pauli operators under conjugation. Specifically, the Hadamard gate  $H$  maps Pauli- $X$  to  $Z$  operators, while  $H_{YZ} = H\sqrt{Z}H$  (both contained in the Clifford group) intertwines between Pauli  $Y$  and  $Z$ . In what follows, the term Clifford deformation will refer to a replacement of a qubit Pauli operator by a different Pauli operator according to one of those conjugations [25].

Any set of operators derived via Clifford deformations—in the form of Clifford conjugations—will form legitimate code stabilizers as long as commutativity is preserved. It turns out that this requirement is fulfilled as a sufficient condition when the stabilizers belonging to the same sub-lattice (different sub-lattices) measure the same Pauli operator (different operators) on the qubits in their common support. In other words, for each given qubit, pairs of Pauli operators located horizontally and vertically from it have to be identical within each pair, but different between the pairs [see Fig. 2 (a)].

**Definition 1** (Consistent Clifford deformation). Denote with  $\sigma_i^s$  the Pauli operator measured on qubit  $i \in L$  by stabilizer  $s$  of the surface code. We call a Clifford conjugation consistent if

$$\sigma_i^{v1} = \sigma_i^{v2} \neq \sigma_i^{h1} = \sigma_i^{h2}, \quad (7)$$

with  $v_k$  ( $h_k$ ) denoting stabilizers located vertically (horizontally) from qubit  $i$ , as illustrated in Fig. 2 (a).

As an example, operators measured at the central qubit  $i \in L$  of Fig. 1 are

$$\begin{aligned} \sigma_i^{v1} &= \sigma_i^{v2} = X_i, \\ \sigma_i^{h1} &= \sigma_i^{h2} = Z_i. \end{aligned} \quad (8)$$

**Lemma 2** (Commutativity). *Consistent Clifford deformations give rise to commuting stabilizers of the surface code.*

*Proof.* It is rather straightforward to check that condition (7) guarantees commutativity of all stabilizers in the code. Firstly, stabilizers that do not have common qubits in their support always commute. Commutativity of stabilizers with one common qubit in their support follows trivially from Eq. (7) and Fig. 2 (a). Finally, the commutator of the neighboring primal and dual stabilizers shown in Fig. 2 (b) reads

$$\begin{aligned} [\sigma_1^h \sigma_2^v, \sigma_1^v \sigma_2^h] &= \sigma_1^h [\sigma_2^v, \sigma_1^v \sigma_2^h] + [\sigma_1^h, \sigma_1^v \sigma_2^h] \sigma_2^v \\ &= \sigma_1^h \sigma_1^v \sigma_2^v \sigma_2^h - \sigma_1^h \sigma_1^v \sigma_2^h \sigma_2^v \\ &\quad + \sigma_1^h \sigma_1^v \sigma_2^h \sigma_2^v - \sigma_1^v \sigma_1^h \sigma_2^h \sigma_2^v \\ &= \sigma_1^h \sigma_1^v \{\sigma_2^v, \sigma_2^h\} - \sigma_2^h \sigma_2^v \{\sigma_1^h, \sigma_1^v\} = 0, \end{aligned} \quad (9)$$

where both anti-commutators of the last line are equal to zero due to condition (7). Since equation (7) applies to each qubit in the code individually, the Pauli operators belonging to a given stabilizer can be chosen independently, e.g., operators  $\sigma_1^h$  and  $\sigma_2^v$  of Fig. 2 (b) belong to the same stabilizer, but can be chosen independently from each other.  $\square$

Therefore, the surface code admits local Clifford deformations that can be chosen independently for each physical qubit. In the focus of this work are new instances of Clifford-deformed surface codes, following up on and building upon Ref. [9]. We start by discussing examples of uniformly deformed surface codes in Sec. 2.3 and subsequently introduce noise-tailored local deformations in Sec. 3.

### 2.3 Surface codes for biased noise

Clifford-deformed surface codes have demonstrated an exceptional performance when physical qubits are affected by biased noise. Consider an error model in

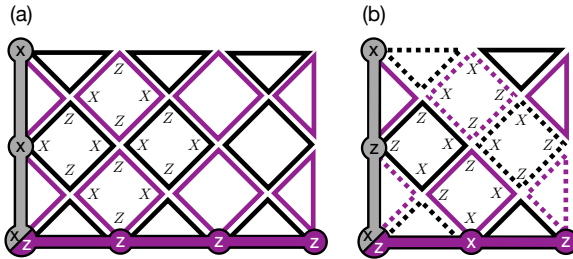


Fig. 3: Surface codes tailored to biased noise in the (a) XZZX and (b) XXZZ configurations. (a) In the XZZX code all stabilizers are identical. Logical  $\bar{X}$  ( $\bar{Z}$ ) operator is shown with solid grey (purple) line and correspond to a product of single-qubit  $X$  ( $Z$ ) Pauli operators. (b) In the XXZZ code the stabilizers with  $(\text{row index} + \text{column index}) = \text{even}$  (solid tiles) differ from the stabilizers with  $(\text{row index} + \text{column index}) = \text{odd}$  (dashed tiles) by interchanging single-qubit  $X$  and  $Z$  Pauli operators. Logical  $\bar{X}$  and  $\bar{Z}$  operators are products of alternating  $X$  and  $Z$  single-qubit Pauli operators.

which each qubit is independently subject to a diagonal *Pauli channel*  $\mathcal{E}$  of the form

$$\mathcal{E}(\rho) := (1-p)\mathbb{1} + xX\rho X + yY\rho Y + zZ\rho Z, \quad (10)$$

where  $x, y, z \in [0, 1]$  are the probabilities of the corresponding single-qubit Pauli error and  $p := x + y + z \in [0, 1]$  is a physical qubit error rate. This being a random unitary process, it is clear that  $\mathcal{E}$  is a valid quantum channel for all allowed parameters. In particular, noise biased towards dephasing corresponds to  $z > x, y$ .

Reference [9] has used a modified surface code, where the transformation  $H_{YZ}$  has been applied to all single-qubit operators of the primal sub-lattice, transforming the plaquette stabilizers to

$$B_{\square} = \prod_{j \in \square} Y_j, \quad (11)$$

which we refer to as the *XY code*. Alternatively, the *XZZX code* [8] can be obtained from the CSS code by applying a Hadamard transformation to Pauli operators on even rows of the code. This effectively replaces both the star and plaquette stabilizers by

$$A_{\diamond} = B_{\square} = X_n Z_e Z_w X_s, \quad (12)$$

where single-qubit Pauli operators acting on north, east, west, and south qubits within each stabilizer, and given the respective indices, are oriented as shown in Fig. 3 (a). These Clifford deformations of the surface code are consistent in the above sense.

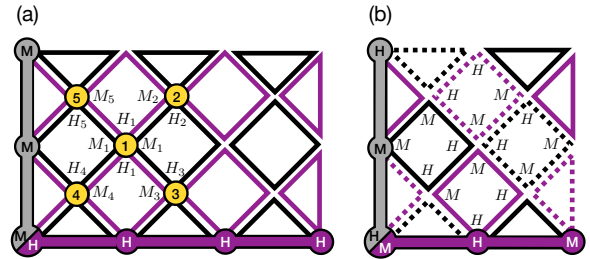


Fig. 4: Noise-tailored surface codes in the (a) MHHM and (b) MMHH configurations. On each given qubit, stabilizers measure Pauli operators corresponding to medium and high rate errors. (a) Operators  $H_i$  and  $M_i$  correspond to high-rate and medium-rate Pauli errors of qubit  $i \in L$  (yellow circles) they are measured on. Stabilizer  $s$  of the MHHM code measures operators  $M_i$  ( $H_i$ ) on qubits  $i$  in the neighborhood of  $s$  located to the east and west (north and south) of it. Logical  $\bar{X}$  and  $\bar{Z}$  operators are products of Pauli operators corresponding to high and medium rate local errors, respectively. (b) As in (a), operators  $M_i$  and  $H_i$  are chosen locally accordingly to error rates of a given qubit. Stabilizers of the MMHH code with  $(\text{row index} + \text{column index}) = \text{even}$  (solid tiles) differ from the stabilizers with  $(\text{row index} + \text{column index}) = \text{odd}$  (dashed tiles) by interchanging operators  $M_i$  and  $H_i$ . For brevity, subscripts of single-qubit operators composing stabilizers of (b) and logical operators in (a,b) are omitted in the figure.

The improved performance of the deformed codes originates from the amount of information available to the decoder. As an illustration, assume an infinitely biased noise described by a *phase-flip channel*

$$\mathcal{E}'(\rho) := (1-p)\mathbb{1} + pZ\rho Z. \quad (13)$$

Since Pauli- $Z$  operators commute with all stabilizers  $B_{\square}$  of the form (1), the primal sub-lattice of the CSS code never detects such error events and hence does not provide any useful information to the decoder. On the other hand, transforming primal stabilizers according to Eq. (11) doubles the amount of useful syndrome information available to the decoder in the XY code. Similarly, Pauli- $Z$  errors create defects in either primal or dual sub-lattice of the XZZX code, depending on which physical qubit has been affected by an error event.

The important difference between the two codes is in the decoder that can be employed to find the correct errors configuration. In the case of the XY code, a single-qubit  $Z$  error event simultaneously creates two pairs of anyons in both sub-lattices. Decoders based on perfect matching behave suboptimally when

decoding such syndrome configurations [10]. Hence, although both the dual and primal sub-lattices of the code contain information about the occurred errors, decoding such configurations require alternative, usually much more computationally demanding methods, such as the maximum likelihood decoding. On the other hand, the same single-qubit  $Z$  error only creates anyons in one of the sub-lattices of the XZZX code at a time, making it well-suited for perfect-matching decoding. Below we will aim at constructing codes that admit efficient decoding with MWPM algorithms as they, due to their fast performance, can potentially be implemented for practical error correction in quantum hardware.

## 2.4 Tailoring aspect ratios

The XZZX code of Fig. 3 (a), i.e., defined on a non-rotated lattice, performs non-optimally on a square-shaped lattice due to the structure of logical operators. For a square surface code of distance  $d$ , the probabilities of logical  $\bar{X}$  and  $\bar{Z}$  errors are  $P^{(\text{sq})}(\bar{X}) = \mathcal{O}(x^d)$  and  $P^{(\text{sq})}(\bar{Z}) = \mathcal{O}(z^d)$ , respectively. Hence, for biased noise with

$$\eta := z/x \gg 1, \quad (14)$$

the logical errors of a square-shaped XZZX code occur predominantly due to the logical  $\bar{Z}$  error,

$$P_{\text{fail}}^{(\text{sq})} \approx P^{(\text{sq})}(\bar{Z}) \gg P^{(\text{sq})}(\bar{X}). \quad (15)$$

The failure rate of the code can be minimized by arranging the qubits on a rectangular lattice with an aspect ratio  $A = d_1/d_2 = \mathcal{O}[\log(z/x)]$ , as in Fig. 3 (a). For a rectangular surface code containing the same number of qubits as a distance- $d$  squared code,

$$d^2 + (d-1)^2 = d_1 d_2 + (d_1 - 1)(d_2 - 1), \quad (16)$$

the logical failure rate obeys

$$P_{\text{fail}}^{(\text{r})} \approx P^{(\text{r})}(\bar{Z}) \approx P^{(\text{r})}(\bar{X}) \ll P_{\text{fail}}^{(\text{sq})}, \quad (17)$$

leading to greatly suppressed logical failure rates in the regime of a large bias. Furthermore, all paths connecting two anyons in the XZZX code are realized with an equal probability

$$P_{i,j} = x^{l_x} z^{l_z} \quad (18)$$

for  $i, j \in L$ . Weights of the input matching decoder graph (4) hence yield a weighted Manhattan distance,

$$w_{i,j} = -\log(x)l_x - \log(z)l_z. \quad (19)$$

For completeness, we introduce an alternative configuration of the surface code that yields optimal logical error rates on a square lattice for arbitrary noise bias. We refer to this code as the XXZZ code owing to the stabilizers configuration shown in Fig. 3 (b). For such a code, logical operators  $\bar{X}$  and  $\bar{Z}$  are products of alternating per-qubit Pauli- $X$  and  $Z$  operators. For sufficiently large lattices, the probabilities of logical errors  $\bar{X}$  and  $\bar{Z}$  are, therefore, approximately equal independently of the noise bias,

$$P^{(\text{sq})}(\bar{X}) \approx P^{(\text{sq})}(\bar{Z}) \approx (xz)^{d/2}. \quad (20)$$

Therefore, the aspect ratio  $A = 1$  can be kept constant for any bias [26]. On the downside, different paths connecting two anyons in the XXZZ code occur with different probabilities. Hence, the matching decoder used in conjunction with the XXZZ code either requires additional computationally demanding pre-processing of input weights, or demonstrates decreased decoding capabilities when the standard Manhattan distance metrics of the form (6) is used to describe the input graph.

## 3 Non-identically distributed errors

In any hardware implementation of a multi-qubit device noise characteristics can vary significantly from one qubit to another. The probabilities of the Pauli channel in Eq. (10) acting on a qubit depend on its  $T_1$  and  $T_2$  times, which vary greatly per qubit on current *noisy intermediate-scale quantum* (NISQ) devices [23, 27–31]. Here, we consider a situation where the probabilities of Pauli errors  $\{x, y, z\}$  are not uniform across qubits labeled  $i \in L$ . Therefore, we assume that noise can be biased towards different types of Pauli errors in different qubits, in a classically known way. Assuming that noise channels of individual qubits can be measured, below we construct a noise-tailored version of the surface code.

Our aim is to consider consistent Clifford deformations such that the most probable syndrome configurations for a given noise model are maximally compatible with perfect-matching decoding. As discussed in the previous section, the efficiency of such an MWPM decoder is compromised by interactions between the primal and dual lattices, i.e., by single-qubit Pauli error events that simultaneously create defects in all four stabilizers surrounding the qubit. One can minimize such events by applying local consistent Clifford deformations introduced earlier in Sec. 2.2.

**Definition 3** (Clifford deformed codes for non-uniform Pauli diagonal noise). Consider qubits located at sites  $i \in L$  subject to Pauli diagonal noise channels with weights  $x_i, y_i, z_i \in [0, 1]$ . Define  $H_i \in \{X_i, Y_i, Z_i\}$  as the Pauli operator reflecting the maximum weight  $h_i := \max\{x_i, y_i, z_i\}$  in the Pauli channel and  $M_i$  as the Pauli operator corresponding to medium weight  $m_i := \max\{x_i, y_i, z_i\} \setminus \{h_i\}$ . The MHMH code measures  $M_i$  ( $H_i$ ) on qubit  $i \in \mathcal{N}_s$  located east and west (north and south) of stabilizer  $s$ , as illustrated in Fig. 4 (a). The MMHH code is similar, but with stabilizers chosen as in Fig. 4 (b).

Here  $\mathcal{N}_s \subset L$  is the set of all qubits in the support of stabilizer  $s$ . As such, if for a given qubit, the Pauli- $X$ ,  $Y$ , or  $Z$  is the least probable Pauli error for a Pauli diagonal noise channel, we modify the surrounding stabilizers such that they measure *different* Pauli operators while maintaining the commutativity condition (7). For qubit  $i$ , the surrounding stabilizers hence measure operators  $M_i$  and  $H_i$ , which correspond to medium and high rate Pauli errors. We refer to two possible layouts of a code locally optimized for perfect-matching decoding as the MHMH [Fig. 4 (a)] and MMHH [Fig. 4 (b)] surface codes due to their similarity to the XZZX [Fig. 3 (a)] and XXZZ [Fig. 3 (b)] codes, respectively.

### 3.1 A paradigmatic toy example

The exact model of how the noise bias varies from one qubit to another depends heavily on a particular hardware implementation of physical qubits. Our aim here is to provide a convincing argument that tailoring the code to local noise structure can be advantageous for decoding. We first demonstrate the proposed scheme on a simple toy model. Assume that the probabilities of low ( $l$ ), medium ( $m$ ), and high-rate ( $h$ ) errors are identical across qubits, but for each qubit located at site  $i \in L$  we choose

$$\{x_i, y_i, z_i\} = \pi_i(\{m, l, h\}), \quad (21)$$

where  $\pi_i$  denotes a random permutation applied at a qubit  $i$ , i.e., for each qubit we randomly assign low, medium, and high rates to different Pauli errors. This is not meant to be a realistic noise model, but has been designed to explain the functioning of the approach, and to ensure that the overall error rate is well defined. Using the known rates of Pauli errors at each individual qubit, one can transform the CSS surface code into the MMHH or MHMH code by applying

local Clifford deformations to it. It is easy to see that the Clifford-deformed MMHH (MHMH) code in the presence of the noise described by Eq. (21) is equivalent to the XXZZ (XZZX) code affected by the noise with  $\pi_i = 1$ . Put another way, noise-informed Clifford deformations effectively undo the permutations applied to errors in Eq. (21).

### 3.2 A more realistic noise model

We will now investigate the code performance in a more realistic error model, where the total error probabilities as well as the relative probabilities of different Pauli errors vary between qubits. For a qubit located at site  $i \in L$  we generate the error probabilities in two steps. First, we choose the error probabilities according to

$$p_i^k \sim \mathcal{N}(0.5, \sigma_P), \quad (22)$$

where  $k = \{X, Y, Z\}$  and  $\mathcal{N}(\mu, \sigma_P)$  is a truncated at 0 and 1 normal distribution with mean  $\mu$  and standard deviation  $\sigma_P$ . Next, we normalize Pauli error probabilities  $p_i^k$  on local error rates  $p_i$  of individual qubits,

$$\sum_{k=X,Y,Z} p_i^k = p_i, \quad (23)$$

where  $p_i$  is also generated according to normal distribution

$$p_i \sim \mathcal{N}(p, p\sigma_{\text{tot}}) \quad (24)$$

for each site  $i \in L$ . This process generates the probabilities of low, medium, and high rate errors independently for each qubit and randomly assigns these probabilities to Pauli errors. Noise in our model is hence characterized by an average error rate  $p$  and a pair of parameters  $\sigma = (\sigma_P, \sigma_{\text{tot}})$  defining, respectively, variations in types of Pauli errors and in total error rates of qubits. We will refer to the noise model described by  $\sigma = (\sigma_P > 0, 0)$  as *uniform total noise*, and to the noise model with  $\sigma = (0, \sigma_{\text{tot}} > 0)$  as *uniform Pauli noise*. A trivial case of  $\sigma = (0, 0)$  corresponds to the iid error model. Knowing the rates of Pauli errors of each qubit, the noise-tailored surface codes can now be constructed according to the patterns of Fig. 4, as in the previous toy example. It is worth noting that in many physically relevant setting, two Pauli error rates are identical, while a third is different, reflecting what is commonly referred to as noise with different  $T_1$  and  $T_2$  times. Even if these errors are distributed in a non-iid fashion, the methods developed here are applicable to this situation as well.

$\sigma_{\text{tot}}$	0	0	0.5	0.5
$\sigma_P$	0	0.5	0	0.5
Manhattan distance metrics				
CSS	0.162	0.163	0.166	0.164
MMHH	0.164	0.185	0.165	0.185
MHHM	0.164	0.187	0.164	0.188
Dijkstra distance metrics				
CSS	0.163	0.168	0.178	0.181
MMHH	0.162	0.190	0.177	0.205
MHHM	0.165	0.190	0.178	0.206

Table 1: Error correction thresholds of different surface codes determined in Appendix A. The first column provides the thresholds observed for a uniform total error model described by  $\sigma = (1/2, 0)$ . The second column corresponds to a non-uniform error rate with  $\sigma = (0, 1/2)$ . In the third column, both total and Pauli error rates vary between qubits. We benchmark the performance of decoders with weights determined according to two distance metrics. The first metric is defined according to the Manhattan distances of Eq. (6) [CSS and MMHH] and Eq. (25) [MHHM]. The second metric uses the known local error rates and calculates shortest weighted paths calculated with Dijkstra algorithm.

### 3.2.1 Noise-aware Clifford deformations

We have numerically simulated and assessed the performances of the CSS code, the XXZZ code, and noise-tailored MHHM and MMHH codes using a modified version of the QECSIM Python package [32]. First, we benchmark the performance of the error correcting codes using a matching decoder with input weights defined according to the Manhattan distance. For square-shaped codes (CSS, XXZZ, MMHH), we use the MWPM algorithm with the standard Manhattan weights calculated as in Eq. (6). The MHHM code performs optimally on a rectangular lattice due to the structure of its logical operators, similarly to the XZZX code under biased noise. Hence, for decoding a syndrome of the MHHM code we use the weighted Manhattan distance metrics similar to Eq. (19),

$$w_{i,j} = -\log \langle p_h \rangle l_x - \log \langle p_m \rangle l_z, \quad (25)$$

where  $\langle p_h \rangle$  and  $\langle p_m \rangle$  are the probabilities of high- and medium-rate errors averaged over all qubits in the code.

Figure 5 (a) demonstrates the comparison between sub-threshold logical error rates of different variants of the surface code versus a code distance  $d$ . The noise-tailored codes clearly demonstrate exponentially suppressed logical failure rates when com-

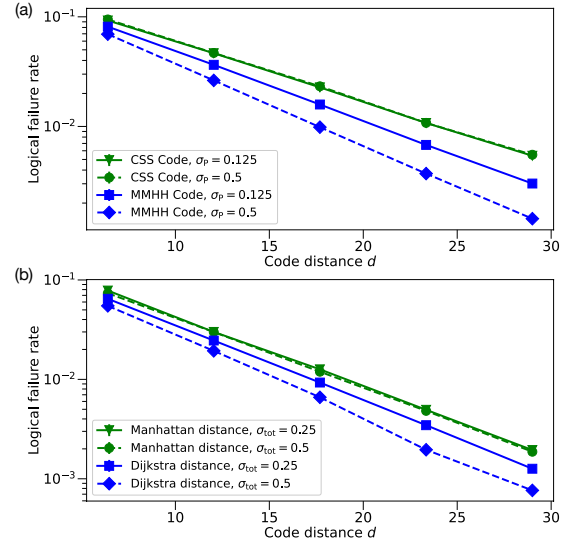


Fig. 5: Sub-threshold logical failure rates vs. code distance  $d$  of squared-shaped surface codes. (a) Tailoring codes stabilizers to local Pauli noise. Green and blue curves correspond to, respectively, the CSS and noise-tailored MMHH codes. The curves are derived using a standard MWPM decoder with the Manhattan distance defined in Eq. (6). Data is shown for  $p = 0.1$  and  $\sigma_{\text{tot}} = 1/2$  in Eq. (22). Dashed and solid lines correspond to  $\sigma_P = 0.125$  and  $\sigma_P = 0.5$ , respectively. The XXZZ and XZZX codes yield logical error rates identical to those of the CSS code, while the MHHM code demonstrates a scaling similar to that of the MMHH code. These curves are hence not shown. (b) Tailoring a matching decoder to local total noise. Green (blue) curve correspond to the MHHM code in conjunction with a decoder using the Manhattan (Dijkstra) distance metrics. Solid and dashed lines correspond to noise models with  $\sigma_{\text{tot}} = 0.25$  and  $\sigma_{\text{tot}} = 0.5$ , respectively.

pared to the CSS and XXZZ codes. We also summarize the error correction thresholds for four descriptive sets of parameters  $\sigma$  in Table 1. We observe that when the code stabilizers are tailored to non-uniform Pauli noise the thresholds are improved as well. As expected, the advantage of using the locally-tailored MHHM and MMHH codes over the CSS and XXZZ codes grows as we increase  $\sigma_P$ , both in terms of thresholds [Fig. 10] and sub-threshold scaling [Fig. 5 (a)]. On the contrary, changing  $\sigma_{\text{tot}}$  does not affect the error correction capabilities of the codes; both the threshold and sub-threshold scaling remain intact as we vary  $\sigma_{\text{tot}}$ . In Appendix A, we explore the decoding capabilities of different codes for a wider range of parameters  $\sigma$  and discuss the thresholds calculation procedure in more detail.

### 3.2.2 Noise-aware matching decoder

The improved performance of the surface code observed in Fig. 5 (a) and Appendix A is achieved solely by adapting the code stabilizers, while the decoder uses the distance metrics of Eqs. (6) and (25). That is, no information about local error rates has been provided to the decoder. However, a decoder can as well be tailored to more reliably decode error syndromes by utilizing the available information about the error model [22]. Here we investigate the behaviour of the surface codes in conjunction with a decoder that uses the local error rates of each qubit. The weights of the matching graph are calculated according to the probabilities of the shortest weighed paths using Dijkstra algorithm, which we implement with the PyMatching package [33].

Our numerical simulations show that implementing a noise-aware decoder instead of the one based on the Manhattan distance does not noticeably improve error correction capabilities of the code against non-uniform Pauli noise, that is, both threshold and sub-threshold scaling are nearly unaffected when we vary  $\sigma_P$  at a fixed  $\sigma_{\text{tot}}$ . In contrast, such a modification yields improvement in the presence of non-uniform total errors, i.e., when we increase  $\sigma_{\text{tot}}$ . As such, Table 1 demonstrates noticeably higher error thresholds enabled by a noise-aware decoder compared to the case of Manhattan distance for  $\sigma_{\text{tot}} = 0.5$ . As we show in Fig. 5 (b), the sub-threshold error rates also scale more favourably when Dijkstra metrics is used, with logical error rate decreasing as  $\sigma_{\text{tot}}$  grows. We explain this behaviour by the fact that errors become less random when  $\sigma_{\text{tot}}$  is increased. As an illustrative example, consider a situation where the total error probabilities of certain qubits are close to zero. In such a case, the decoder knows that errors should not take place on these qubits and makes a more informative decision about locations of errors, resulting in more accurate decoding. For a detailed comparison of the two decoders, we refer the reader to Appendix B and figures therein.

### 3.2.3 Non-uniform error correction

Summarizing this Section, we considered two types of non-uniformity in qubit noise: variation in Pauli noise and variation in total qubit noise. We have shown that the former can be countered by applying noise-aware Clifford deformations to the code stabilizers, and the latter can be corrected more efficiently by making the decoder noise-aware. The ad-

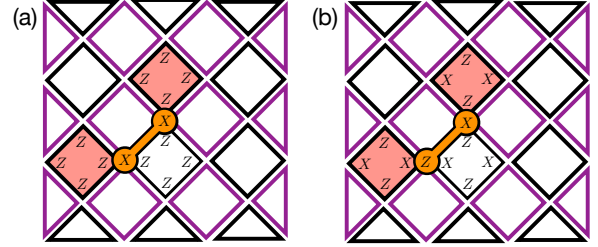


Fig. 6: Surface codes tailored for a known two-qubit noise channel. (a) Two-qubit phase-flip and bit-flip errors between nearest neighbors create anyons within one of the sub-lattices, as shown with salmon tiles, and can be efficiently decoded. (b) In the presence of, e.g., XZ correlations, the code stabilizers can be Clifford-deformed to maintain the same decoding capabilities as in (a).

vantage of tailoring the code stabilizers become more apparent as we introduce stronger variations in Pauli noise (increase  $\sigma_P$ ), while using the noise-aware decoder becomes more advantageous as we introduce stronger variations in total noise (increase  $\sigma_{\text{tot}}$ ). Importantly, the modifications to the code stabilizers and the decoder input weights are independent and can hence be implemented simultaneously. Further steps can be made along the same lines of research. As such, local Clifford deformations can in principle be combined with belief propagation or belief matching [11]. Such decoding strategies might lead to an improved accuracy, but are likely to be much more computationally demanding than the fast matching decoder used in our simulations. Hence, we leave the question of designing alternative decoding algorithms outside of the scope of this paper.

## 4 Correlated errors and code degeneracy

We now turn to the case where correlated errors are present between pairs of nearest-neighbor qubits. We focus on this particular case because of two reasons. Firstly, only two-qubit correlations can occur as a result of the coherent evolution. Assuming that errors due to decoherent processes are weak, it suffices to consider only pairwise correlations. Secondly, as discussed in Ref. [16], correlated errors on pairs of qubits which are not nearest neighbors are expected to have less destructive effect on the error correction fidelity.

The dynamics of the surface code in the presence

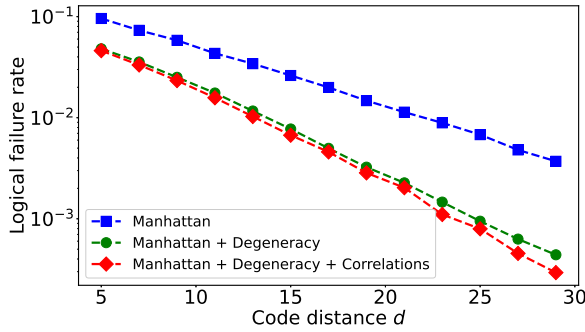


Fig. 7: Simulated logical error rates versus code distance in the presence of nearest-neighbor correlations. Qubits are affected by a combination of single-qubit depolarizing noise and local two-qubit XZ errors. Code stabilizers are constructed according to Fig. 3, i.e., we use the XZZX code to efficiently correct the correlated errors. Blue (squares) curve corresponds to the MWPM with edges weighted according to the standard Manhattan distance (6). Green (circles) curve corresponds to the weights that take syndrome degeneracy into account, i.e., defined according to Eq. (35). Red (diamonds) curve corresponds to a decoder that explicitly takes into account the probability of two-qubit errors, as in Eq. (31). Data is shown for  $p = 0.125$  and  $p_1 = 0.25p$ .

of correlated nearest-neighbor errors has been previously studied in Ref. [16]. Here, the authors have considered qubits subject to a combination of single- and two-qubit bit-flip error channels that read

$$\mathcal{E}_m^{(1)}(\rho) = X_m \rho X_m \quad (26)$$

and

$$\mathcal{E}_m^{(2)}(\rho) = \sum_{l \in \mathcal{N}_m} X_m X_l \rho X_m X_l, \quad (27)$$

respectively. Again,  $\mathcal{N}_m \subset L$  is a set of all nearest neighbors of  $m \in L$ . The total noise channel affecting qubit  $m$  is then described by a quantum channel

$$\begin{aligned} \mathcal{E}''(\rho) &= (1 - p_1 - p_2)\rho \\ &+ p_1 \mathcal{E}_m^{(1)}(\rho) + p_2 \mathcal{E}_m^{(2)}(\rho), \end{aligned} \quad (28)$$

where  $p_1$  and  $p_2$  are the probabilities of single- and two-qubit errors, respectively. In Ref. [16], the authors have shown that the performance of a matching decoder can be improved by modifying the weights in Eq. (4) such that both single- and two-qubit error probabilities are taken into account. In a weakly interacting regime  $p_2/p_1 \ll 1$ , the probability of connecting two defects via the most probable chain of single-qubit errors reads

$$P_1 = \binom{l_x + l_z}{l_x} p_1^{l_x + l_z}, \quad (29)$$

which is identical to Eq. (4) up to a degeneracy pre-factor that takes into account the number of shortest paths between two stabilizers.

The probability of connecting the defects via a chain of two-qubit errors can be deduced from Fig. 6 (a) and reads

$$P_2 = \binom{l_m}{(l_x + l_z)/2} p_2^{l_m}, \quad (30)$$

where  $l_m = \max(l_x, l_z)$ . The adjusted MWPM weights can then be approximated by taking into account syndrome degeneracies and two-qubit correlated errors by

$$w_{i,j}^{(\text{deg+corr})} = -\log(P_1 + P_2), \quad (31)$$

which is valid to the lowest order in the limits of weak ( $p_2/p_1 \ll 1$ ) and strong ( $p_2/p_1 \gg 1$ ) coupling regimes [34].

As shown in Fig. 6 (a), the standard CSS surface code used in conjunction with a MPWM decoder is well suited for correcting correlated bit-flip errors since such errors create anyons only within one sub-lattice at a time, giving a rise to the probability of the form (30). The same applies to an arbitrary combination of correlated bit-flip and phase-flip errors described by a superoperator

$$\begin{aligned} \mathcal{E}_m^{(2)}(\rho) &= p_{XX} \sum_{l \in \mathcal{N}_m} X_m X_l \rho X_m X_l \\ &+ p_{ZZ} \sum_{l \in \mathcal{N}_m} Z_m Z_l \rho Z_m Z_l, \end{aligned} \quad (32)$$

where  $p_{XX} \in [0, 1]$  and  $p_{ZZ} = 1 - p_{XX}$  are the fractions of bit-flip and phase-flip errors in the total two-qubit error channel, respectively. Since the first (second) term of Eq. (32) commutes with star (plaquette) stabilizers of Eq. (1), a single error event creates defects in only one sub-lattice of the code, making a syndrome efficiently decodable by a matching algorithm.

In contrast, two-qubit correlations of XZ-type read

$$\begin{aligned} \mathcal{E}_m^{(2)}(\rho) &= \frac{1}{2} \sum_{l \in \mathcal{N}_m} (X_m Z_l \rho Z_m X_l \\ &+ Z_m X_l \rho X_m Z_l) \end{aligned} \quad (33)$$

and create four defects in both primal and dual sub-lattices of the CSS code, hence compromising the performance of a matching decoder. To maintain the compatibility with a decoder, the code can be Clifford-deformed. For example, as we show in

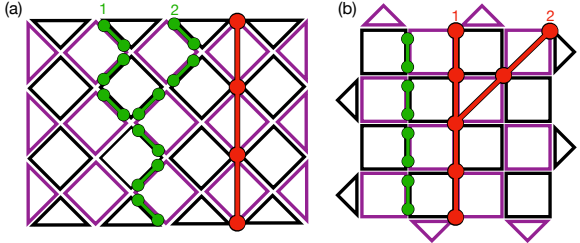


Fig. 8: Examples of logical  $\bar{Z}$  operators of the (a) non-rotated and (b) rotated surface codes constructed according to Fig. 6, i.e., such that a single two-qubit error only creates defects in one of the sub-lattices. Single- and two-qubit errors are shown schematically with red dots and green dumbbells, respectively. In (a), single-qubit error can form only  $d$  different shortest-path logical operators, while the number of shortest-path logical operators formed by two-qubit errors is highly degenerate. For the rotated surface code of (b), the situation is reversed, i.e., the number of logical errors due to single-qubit errors is highly degenerate.

Fig. 6 (b), the XZZX obeys the same dynamics under XZ correlations as the CSS code under two-qubit bit-flip and phase-flip channel (32). The surface code compatibility with the matching decoder is hence improved by Clifford deformation, similarly to the case of a non-uniform noise investigated in the previous section.

We numerically investigate the performance of the XZZX surface code in the presence of single-qubit depolarizing noise described by

$$\mathcal{E}_i^{(1)}(\rho) = \frac{1}{3} \sum_{k=X,Y,Z} \sigma_i^k \rho \sigma_i^k \quad (34)$$

and two-qubit depolarizing noise of the form (33). In Eq. (34),  $\sigma_i^k$  denotes Pauli- $k$  operator applied to qubit  $i$ . Fig. 7 shows the simulated sub-threshold error rates for three different cases: (i) when the decoder uses the standard Manhattan weights of Eq. (6), (ii) for the weights calculated according to Eq. (31), and (iii) when the term  $P_2$  in Eq. (31) is ignored. As seen in the figure, MPWM decoder with input graph weights defined according to (ii), i.e., with both correlations and code degeneracy taken into account, yields exponentially suppressed sub-threshold logical failure rates compared to case (i) when a standard Manhattan metrics is used.

Our simulations, however, show a surprising feature of error correction in the presence of correlated two-qubit noise: the term  $P_2$  in Eq. (30) is, in fact, redundant, and ignoring it as in case (iii) has vanishingly small effect on decoding capabilities of the de-

coder. Instead, merely accounting for syndrome degeneracy in Eq. (29) is responsible for the suppressed logical error rates. Ignoring the probability of connecting two defects by a chain of two-qubit errors, Eq. (31) yields

$$w_{i,j}^{\text{deg}} = l_x + l_y - \log \left( \frac{l_x + l_y}{l_x} \right), \quad (35)$$

where we have omitted a constant shift  $-\log p_1 > 0$ . As we show in Fig. 7, matching decoders with weights defined according to Eqs. (31) and (35) perform nearly identically, meaning that no information about the magnitudes of single- and two-qubit noise is required by the decoder to efficiently decode a syndrome in the presence of correlated two-qubit noise.

We explain the role of syndrome degeneracy in decoding two-qubit errors by degeneracy of logical operators that such errors can produce. A similar argument has recently been provided in Ref. [35] for single-qubit errors affecting the standard (i.e., non-rotated) and rotated surface codes. Let us first consider independent single-qubit errors. Fig. 8 shows examples of logical operators realized by shortest chains of single-qubit errors in non-rotated and rotated surface code geometries. While the former only supports  $d$  such logical errors, the latter can support a much larger number of them due to a high degree of logical operator degeneracy. Ref. [35] has shown that taking syndrome degeneracy into account improves the decoding accuracy for the case of rotated surface code, but has little to no effect in non-rotated codes, which agrees well with our numerical simulations provided in Appendix C. The authors of Ref. [35] attribute the difference in effect that syndrome degeneracy has on decoding to degeneracy of logical operators that can be produced by single-qubit errors.

A similar, but opposite effect takes place when correlated errors are present in the system: local two-qubit errors form highly-degenerate shortest-path logical operators in the non-rotated code, while the rotated code only supports  $d$  shortest two-qubit chains, see Fig. 8. Hence, taking the degeneracy into account in Eq. (35) has a positive effect of decoding two-qubit errors in the non-rotated surface code, which agrees with the results of Fig. 7. Following the same logic, one can expect that taking degeneracy into account for decoding similar correlated errors in the rotated code will have negligible effect of the accuracy. This also agrees well with our numerical simulations provided in Appendix C. Hence, taking code degeneracy into account plays a similar role

for decoding single-qubit error on the rotated code as for decoding two-qubit error on the non-rotated code. Put another way, turning on correlated errors can be thought of as partial rotation of the code in the context of logical operator degeneracy.

As we have shown above, an MWPM decoder can efficiently handle correlated nearest-neighbor errors of certain types without the need of adjusting the decoding procedure to a known structure of the noise. Instead, merely taking syndrome degeneracy into account effectively adjusts the matching decoder to a noise model. Physical qubits in the surface code can in principle be affected by correlated errors other than two-qubit Pauli errors. In the future, it will be interesting to investigate if a similar argument holds when qubits are affected by different correlated errors of different structures.

## 5 Conclusion

In conclusion, we have studied the performance of Clifford-deformed surface codes in the presence of non-identically distributed and correlated two-qubit errors. In both cases the sub-threshold logical error rates are shown to be exponentially suppressed compared to the standard CSS codes. Importantly, the improved decoding accuracy is achieved using a fast matching decoder that does not require numerically extensive pre-processing and can potentially be implemented in real quantum hardware. We have studied the performance of matching decoders with input parameters defined according to different distance metrics and shown the advantage of using the shortest weighted paths as graph weights in the case of non-uniform qubit error rates. Our aim has been to demonstrate the principle of noise-tailored local Clifford deformations. To this aim, we have used simple error models as test cases. This can be seen as a further substantial step towards designing physics non-agnostic codes for quantum error correction. Finally, we have investigated the connection between code degeneracy and structures of the noise affecting qubits in the rotated and non-rotated surface code configurations. This in turn allowed us to identify cases where taking code degeneracy into account has a positive effect on decoding accuracy.

In this work, we have considered the performance of noise-tailored surface codes for simple *code capacity* noise models where only the data qubits are subject to error. As a direction for further work, it would be interesting to investigate noise-tailored

codes under more realistic circuit level noise models for which it is assumed every location in the error correction circuit has the potential to introduce errors. In a previous study [11], Higgott *et al.* have proposed the belief-matching decoder as a heuristic for circuit-level decoding of the XY-surface code. The results of [11] suggest that some of the advantages of bias-tailoring are reduced under circuit-level noise due to boundary effects. However, it is possible that the more precisely tailored MHHM and MMHH codes proposed in this work could be free of such failure modes.

In the future, it will also be interesting to apply the proposed ideas to even more realistic error models that faithfully reflect noise processes in various hardware implementations of qubits. The notion of consistent Clifford deformations makes sense also for other *topological quantum error correcting codes* beyond the toric or surface codes. Many of the developed ideas of Clifford-deformed codes beyond the iid setting readily carry over to other codes as well, giving rise to new sets of commuting stabilizers that are adapted to the noise model. It also seems perfectly conceivable that *coherent errors* can be addressed in a way similar to the one described here. Additionally, it would be interesting to investigate the influence of Clifford deformations on the performance of other decoders such as the union find decoder and belief matching. It is the hope that the present work can contribute to the line of thought of bringing notions of quantum error correction closer to ideas on actual quantum hardware development, and to think about quantum error correction in more physically motivated terms.

## Acknowledgments

We gratefully acknowledge funding by the Federal Ministry of Education and Research (BMBF) via the RealistiQ project (13N15580), for which this is a joint work between the two project partners. J. E. has also been funded by the Federal Ministry of Education and Research (BMBF) under QSolid and MUNIQC-ATOMS as well as by the DFG (CRC 183). The project is also part of the Munich Quantum Valley (K8), which is supported by the Bavarian state government with funds from the Hightech Agenda Bayern Plus. The authors thank the HPC Service of ZEDAT, Freie Universität Berlin, for offering computing time [36].

## Data availability

The data and the code that generates the plots within this paper are available at [37].

## References

- [1] K. J. Satzinger, Y.-J. Liu, A. Smith, C. Knapp, M. Newman, C. Jones, Z. Chen, C. Quintana, X. Mi, A. Dunsworth, C. Gidney, I. Aleiner, F. Arute, K. Arya, J. Atalaya, R. Babbush, J. C. Bardin, R. Barends, J. Basso, A. Bengtsson, A. Bilmes, M. Broughton, B. B. Buckley, D. A. Buell, B. Burkett, N. Bushnell, B. Chiaro, R. Collins, W. Courtney, S. Demura, A. R. Derk, D. Eppens, C. Erickson, L. Faoro, E. Farhi, A. G. Fowler, B. Foxen, M. Giustina, A. Greene, J. A. Gross, M. P. Harrigan, S. D. Harrington, J. Hilton, S. Hong, T. Huang, W. J. Huggins, L. B. Ioffe, S. V. Isakov, E. Jeffrey, Z. Jiang, D. Kafri, K. Kechedzhi, T. Khattar, S. Kim, P. V. Klimov, A. N. Korotkov, F. Kostritsa, D. Landhuis, P. Laptev, A. Locharla, E. Lucero, O. Martin, J. R. McClean, M. McEwen, K. C. Miao, M. Mohseni, S. Montazeri, W. Mruczkiewicz, J. Mutus, O. Naaman, M. Neeley, C. Neill, M. Y. Niu, T. E. O'Brien, A. Opremcak, B. Pató, A. Petukhov, N. C. Rubin, D. Sank, V. Shvarts, D. Strain, M. Szalay, B. Villalonga, T. C. White, Z. Yao, P. Yeh, J. Yoo, A. Zalcman, H. Neven, S. Boixo, A. Megrant, Y. Chen, J. Kelly, V. Smelyanskiy, A. Kitaev, M. Knap, F. Pollmann, and P. Roushan, *Science* **374**, 1237 (2021).
- [2] D. Nigg, M. Müller, E. A. Martinez, P. Schindler, M. Hennrich, T. Monz, M. A. Martin-Delgado, and R. Blatt, *Science* **345**, 302 (2014).
- [3] S. Krinner, N. Lacroix, A. Remm, A. D. Paolo, E. Genois, C. Leroux, C. Hellings, S. Lazar, F. Swiadek, J. Herrmann, G. J. Norris, C. K. Andersen, M. Müller, A. Blais, C. Eichler, and A. Wallraff, *Nature* **605**, 669–674 (2022).
- [4] C. Ryan-Anderson, J. G. Bohnet, K. Lee, D. Gresh, A. Hankin, J. P. Gaebler, D. Francois, A. Chernoguzov, D. Lucchetti, N. C. Brown, T. M. Gatterman, S. K. Halit, K. Gilmore, J. Gerber, B. Neyenhuis, D. Hayes, and R. P. Stutz, (2021), arXiv:2107.07505 .
- [5] A. Acín, I. Bloch, H. Buhrman, T. Calarco, C. Eichler, J. Eisert, J. Esteve, N. Gisin, S. J. Glaser, F. Jelezko, S. Kuhr, M. Lewenstein, M. F. Riedel, P. O. Schmidt, R. Thew, A. Wallraff, I. Walmsley, and F. K. Wilhelm, *New J. Phys.* **20**, 080201 (2018).
- [6] J. Lee, J. Park, and J. Heo, *Quantum Information Processing* **20**, 231 (2021).
- [7] A. Dua, A. Kubica, L. Jiang, S. T. Flammia, and M. J. Gullans, (2022), arXiv:2201.07802 .
- [8] J. P. Bonilla Ataides, D. K. Tuckett, S. D. Bartlett, S. T. Flammia, and B. J. Brown, *Nature Comm.* **12**, 2172 (2021).
- [9] D. K. Tuckett, S. D. Bartlett, and S. T. Flammia, *Phys. Rev. Lett.* **120**, 050505 (2018).
- [10] D. K. Tuckett, S. D. Bartlett, S. T. Flammia, and B. J. Brown, *Phys. Rev. Lett.* **124**, 130501 (2020).
- [11] O. Higgott, T. C. Bohdanowicz, A. Kubica, S. T. Flammia, and E. T. Campbell, (2022), arXiv:2203.04948 .
- [12] D. K. Tuckett, A. S. Darmawan, C. T. Chubb, S. Bravyi, S. D. Bartlett, and S. T. Flammia, *Phys. Rev. X* **9**, 041031 (2019).
- [13] A. S. Darmawan, B. J. Brown, A. L. Grimsmo, D. K. Tuckett, and S. Puri, *PRX Quantum* **2**, 030345 (2021).
- [14] J. O'Gorman, N. H. Nickerson, P. Ross, J. J. Morton, and S. C. Benjamin, *npj Quant. Inf.* **2**, 15019 (2016).
- [15] A. Mizel and D. A. Lidar, *Phys. Rev. B* **70**, 115310 (2004).
- [16] A. Hutter and D. Loss, *Phys. Rev. A* **89**, 042334 (2014).
- [17] P. Baireuther, T. E. O'Brien, B. Tarasinski, and C. W. J. Beenakker, *Quantum* **2**, 48 (2018).
- [18] J. P. Clemens, S. Siddiqui, and J. Geabanacloche, *Phys. Rev. A* **69**, 062313 (2004).
- [19] D. Aharonov, A. Kitaev, and J. Preskill, *Phys. Rev. Lett.* **96**, 050504 (2006).
- [20] A. G. Fowler and J. M. Martinis, *Phys. Rev. A* **89**, 032316 (2014).
- [21] P. Jouzdani, E. Novais, I. S. Tupitsyn, and E. R. Mucciolo, *Phys. Rev. A* **90**, 042315 (2014).
- [22] A. d. iOlius, J. E. Martinez, P. Fuentes, P. M. Crespo, and J. Garcia-Frias, (2022), arXiv:2203.15695 .
- [23] J. E. Martinez, P. Fuentes, A. d. iOlius, J. Garcia-Frias, J. R. Fonollosa, and P. M. Crespo, (2022), arXiv:2207.06838 .
- [24] G. Smith and J. A. Smolin, *Phys. Rev. Lett.* **98**, 030501 (2007).

- [25] For coherent noise, one could also consider more general Clifford conjugations, either by other unitaries from  $C_1/U(1)$ , or by conjugating several qubits at once and considering  $C_n/U(1)$  for  $n \geq 1$ . Such code deformations will not be considered here.
- [26] Such a XXZZ code is reminiscent to the rotated XZZX code introduced in Ref. [8] that has the same structure of logical operators as in our XXZZ code and therefore also performs optimally on a squared rotated lattice.
- [27] S. S. Tannu and M. K. Qureshi, in *Proceedings of the Twenty-Fourth International Conference on Architectural Support for Programming Languages and Operating Systems*, ASPLOS '19 (Association for Computing Machinery, New York, NY, USA, 2019) p. 987–999.
- [28] Y. Wu, W.-S. Bao, S. Cao, F. Chen, M.-C. Chen, X. Chen, T.-H. Chung, H. Deng, Y. Du, D. Fan, M. Gong, C. Guo, C. Guo, S. Guo, L. Han, L. Hong, H.-L. Huang, Y.-H. Huo, L. Li, N. Li, S. Li, Y. Li, F. Liang, C. Lin, J. Lin, H. Qian, D. Qiao, H. Rong, H. Su, L. Sun, L. Wang, S. Wang, D. Wu, Y. Xu, K. Yan, W. Yang, Y. Yang, Y. Ye, J. Yin, C. Ying, J. Yu, C. Zha, C. Zhang, H. Zhang, K. Zhang, Y. Zhang, H. Zhao, Y. Zhao, L. Zhou, Q. Zhu, C.-Y. Lu, C.-Z. Peng, X. Zhu, and J.-W. Pan, *Phys. Rev. Lett.* **127**, 180501 (2021).
- [29] J. Golden, A. Bärtschi, D. O’Malley, and S. Eidenbenz, *ACM Trans. Quant. Comp.* **3** (2022), 10.1145/3510857.
- [30] F. Arute, K. Arya, R. Babbush, D. Bacon, J. C. Bardin, R. Barends, R. Biswas, S. Boixo, F. G. S. L. Brando, D. A. Buell, B. Burkett, Y. Chen, Z. Chen, B. Chiaro, R. Collins, W. Courtney, A. Dunsworth, E. Farhi, B. Foxen, A. Fowler, C. Gidney, M. Giustina, R. Graff, K. Guerin, S. Habegger, M. P. Harrigan, M. J. Hartmann, A. Ho, M. Hoffmann, T. Huang, T. S. Humble, S. V. Isakov, E. Jeffrey, Z. Jiang, D. Kafri, K. Kechedzhi, J. Kelly, P. V. Klimov, S. Knysh, A. Korotkov, F. Kostritsa, D. Landhuis, M. Lindmark, E. Lucero, D. Lyakh, S. Mandrà, J. R. McClean, M. McEwen, A. Megrant, X. Mi, K. Michelsen, M. Mohseni, J. Mutus, O. Naaman, M. Neeley, C. Neill, M. Y. Niu, E. Ostby, A. Petukhov, J. C. Platt, C. Quintana, E. G. Rieffel, P. Roushan, N. C. Rubin, D. Sank, K. J. Satzinger, V. Smelyanskiy, K. J. Sung, M. D. Trevithick, A. Vainsencher, B. Villalonga, T. White, Z. J. Yao, P. Yeh, A. Zalcman, H. Neven, and J. M. Martinis, *Nature* **574**, 505 (2019).
- [31] F. Arute, K. Arya, R. Babbush, D. Bacon, J. C. Bardin, R. Barends, A. Bengtsson, S. Boixo, M. Broughton, B. B. Buckley, D. A. Buell, B. Burkett, N. Bushnell, Y. Chen, Z. Chen, Y.-A. Chen, B. Chiaro, R. Collins, S. J. Cotton, W. Courtney, S. Demura, A. Derk, A. Dunsworth, D. Eppens, T. Eckl, C. Erickson, E. Farhi, A. Fowler, B. Foxen, C. Gidney, M. Giustina, R. Graff, J. A. Gross, S. Habegger, M. P. Harrigan, A. Ho, S. Hong, T. Huang, W. Huggins, L. B. Ioffe, S. V. Isakov, E. Jeffrey, Z. Jiang, C. Jones, D. Kafri, K. Kechedzhi, J. Kelly, S. Kim, P. V. Klimov, A. N. Korotkov, F. Kostritsa, D. Landhuis, P. Laptev, M. Lindmark, E. Lucero, M. Marthaler, O. Martin, J. M. Martinis, A. Maruszyk, S. McArdle, J. R. McClean, T. McCourt, M. McEwen, A. Megrant, C. Mejuto-Zaera, X. Mi, M. Mohseni, W. Mruczkiewicz, J. Mutus, O. Naaman, M. Neeley, C. Neill, H. Neven, M. Newman, M. Y. Niu, T. E. O’Brien, E. Ostby, B. Pató, A. Petukhov, H. Putterman, C. Quintana, J.-M. Reiner, P. Roushan, N. C. Rubin, D. Sank, K. J. Satzinger, V. Smelyanskiy, D. Strain, K. J. Sung, P. Schmitteckert, M. Szalay, N. M. Tubman, A. Vainsencher, T. White, N. Vogt, Z. J. Yao, P. Yeh, A. Zalcman, and S. Zanker, (2020), arXiv:2010.07965 .
- [32] D. K. Tuckett, *Tailoring surface codes: Improvements in quantum error correction with biased noise*, Ph.D. thesis, University of Sydney (2020), (qecsim: <https://github.com/qecsim/qecsim>).
- [33] O. Higgott, ACM Trans. Quant. Comp. (2021).
- [34] In Eq. (31), we only include the zeroth order terms in  $p_1$  and  $p_2$ . In Ref. [16], the probability of connecting two defects by a chain of single- and two-qubit errors has been calculated to the higher order. That is, the authors have also included the possibility of creating connecting two defects with Manhattan distance  $N$  by one single-qubit error and  $N - 1$  two-qubit errors when  $p_1/p_2 \ll 1$  (by one two-qubit error and  $N - 1$  single-qubit errors when  $p_2/p_1 \ll 1$ ). However, our simulations show that adding such higher-order terms has vanishingly small effect on the decoding fidelity.

- [35] B. Criger and I. Ashraf, *Quantum* **2**, 102 (2018).
- [36] L. Bennett, B. Melchers, and B. Proppe, “Curta: A general-purpose high-performance computer at ZEDAT, Freie Universität Berlin,” (2020).
- [37] “<https://github.com/peter-janderks/plots-and-data-non-iid-errors-with-surface-codes/>” .
- [38] C. Wang, J. Harrington, and J. Preskill, *Ann. Phys.* **303**, 31 (2003).
- [39] J. W. Harrington, *Analysis of quantum error-correcting codes: symplectic lattice codes and toric codes*, Ph.D. thesis, California Institute of Technology (2004).
- [40] R. Sweke, P. Boes, N. H. Y. Ng, C. Sparaciari, J. Eisert, and M. Goihl, *Commun. Phys.* **5**, 150 (2022).

## A Error thresholds calculation

We obtain the threshold estimates of Table 1 using the critical exponent method described in Refs. [38, 39]. Specifically, for physical error rates near the threshold we fit the logical error rate to the function  $P_{\text{fit}} : \mathbb{R}^+ \rightarrow \mathbb{R}$  with

$$P_{\text{fit}}(x) = B_0 + B_1 x + B_2 x^2, \quad (36)$$

where

$$x := (p - p_{\text{th}})^{\alpha d^\beta}. \quad (37)$$

Here,  $d$  is the code distance,  $p$  is the single-qubit error rate, and  $B_0, B_1, B_2, \alpha, \beta$  are fitting parameters.

Figure 9 shows near-threshold logical failure rates and threshold estimates of different codes. The thresholds are also summarized in Table 1. We see that the noise-tailored surface codes demonstrate error correcting thresholds exceeding those of the CSS code by  $\approx 2.3\%$  for  $\sigma_P = 0.5$ . In Fig. 10 we compare the thresholds of the codes for a wider range of values  $\sigma_P$ . We observe increasing thresholds of the noise-tailored codes as  $\sigma_P$  grows. On the other hand, we see little to no difference between error thresholds derived for non-uniform ( $\sigma_{\text{tot}} = 0.5$ ) and uniform ( $\sigma_{\text{tot}} = 0$ ) total error rates, meaning that Clifford deformations do not help with correcting variations in total error rates.

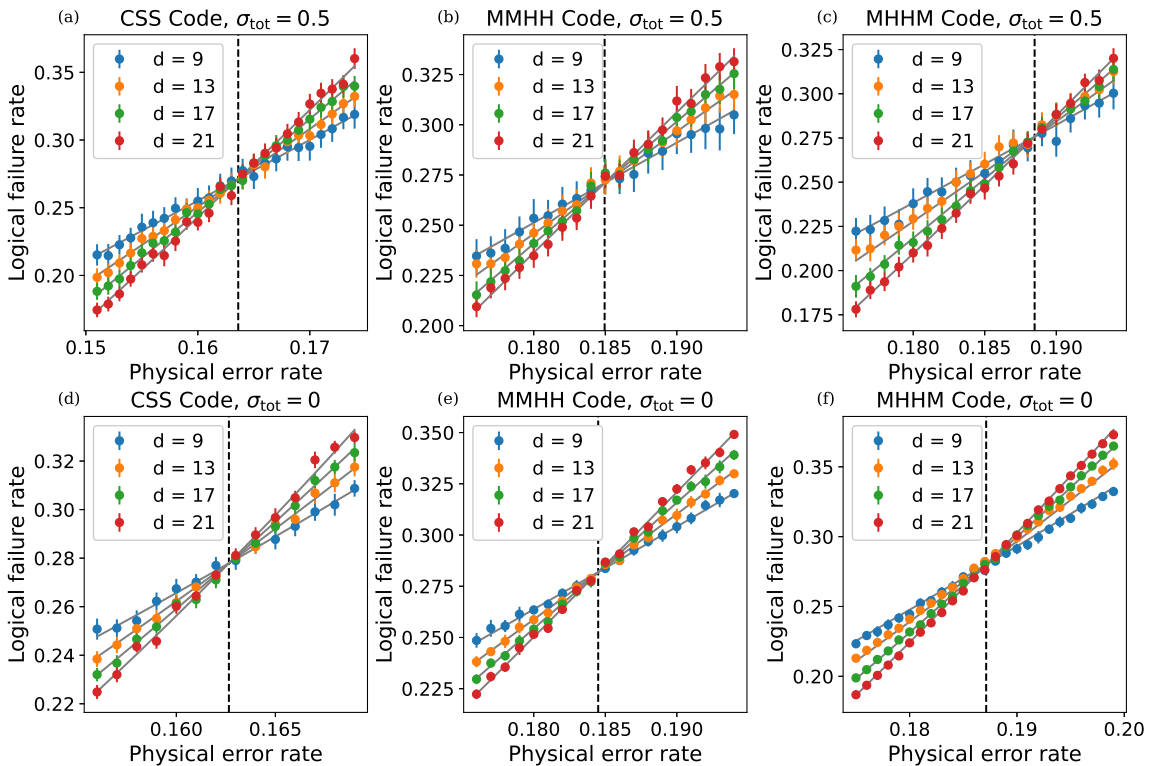


Fig. 9: Logical error rates of the (a,d) CSS and (b,e) MMHH, and (c,f) MHHM surface codes in the presence of affected by non-identically distributed Pauli errors with  $\sigma_P = 0.5$ . In panels (a)–(c) the total qubit noise is nonuniform with  $\sigma_{\text{tot}} = 0.5$ . In panels (d)–(f) the total qubit noise is uniform. The syndromes are decoded using MWPM with distance metric calculated according to the Manhattan distance. Error bars show one standard deviation.

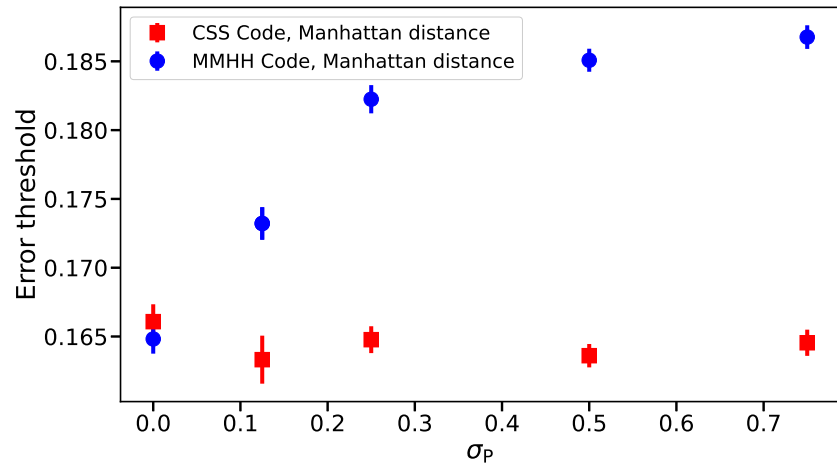


Fig. 10: Error correction thresholds of the CSS (red squares) and MMHH (blue circles) surface codes versus the standard deviation  $\sigma_P$  in Eq. (22) with  $\sigma_{\text{tot}} = 1/2$ . Thresholds are calculated using a MWPM matching decoder with input weights defined according to the Manhattan distance. The threshold of the MMHH increases with the variation in relative Pauli noise described by  $\sigma_P$ , while the threshold of the CSS code remains constant.

## B Shortest-path matching

Figure 11 provides estimation of the error-correction threshold of different codes in the case when we use a noise-aware decoder and define the input weights according to the Dijkstra distance. In contrast to the decoder that uses Manhattan distance metrics, the decoder with Dijkstra-based metrics demonstrates a clear improvement of the error correction thresholds as  $\sigma_{\text{tot}}$  grows, see Figs. 11 and 12.

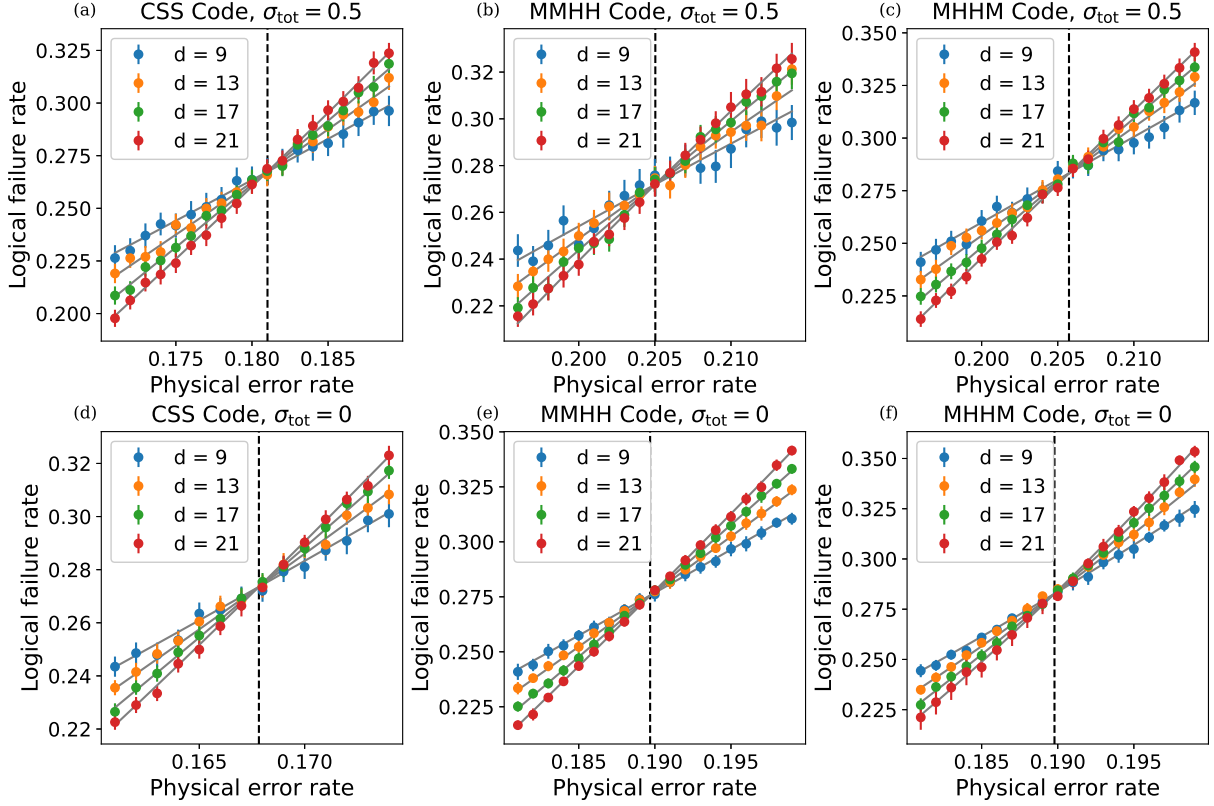


Fig. 11: Same as Fig. 9, but for a matching decoder that uses input weights defined according to the shortest weighted paths. The parameters of the noise used for simulations are identical to those used in Fig. 9.

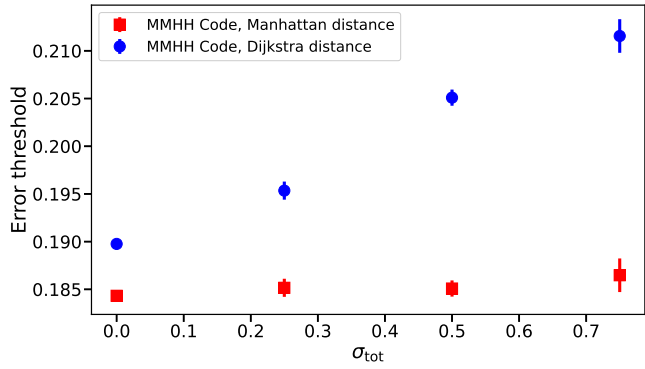


Fig. 12: Error correction thresholds of the MMHH code versus the standard deviation of the total error rate  $\sigma_{\text{tot}}$  in Eq. (24) with  $\sigma_P$ . Red circles and blue squares correspond to matching decoders that use input weights defined according to the Manhattan and Dijkstra distance metrics, respectively. Other codes demonstrate qualitatively similar behaviour and are not shown.

### C Code geometry and syndrome degeneracy

In Fig. 13, we investigate the impact of code geometry and syndrome degeneracy. One can observe a qualitatively opposite behaviour when degeneracy is accounted for decoding error syndromes in rotated and non-rotated surface codes.

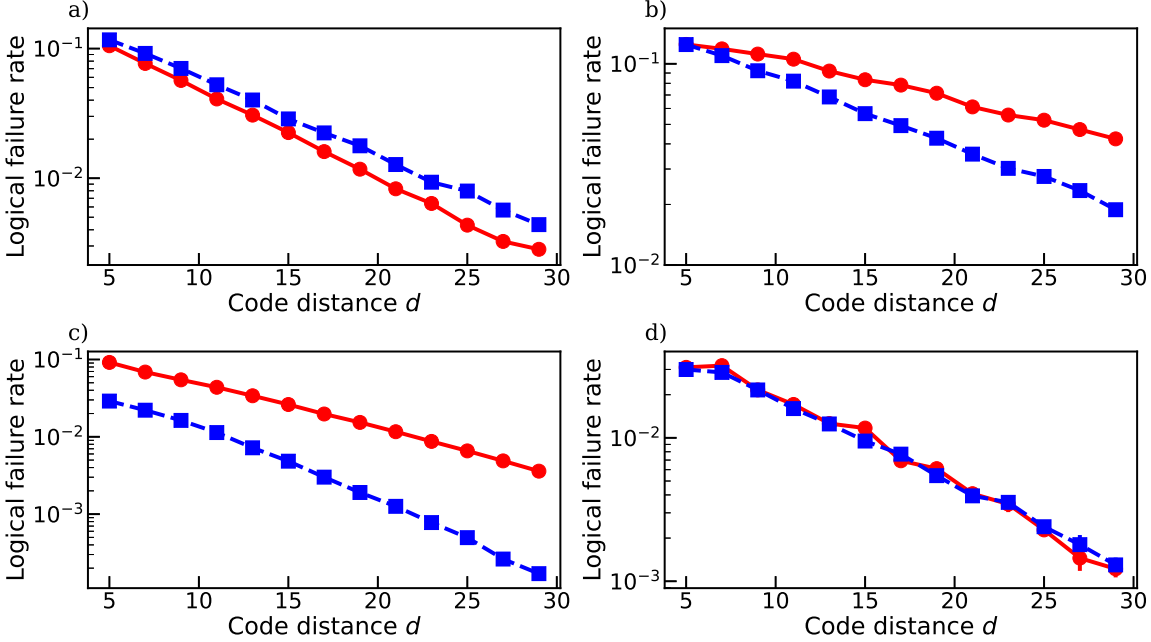


Fig. 13: Numerically simulated logical failure rates of the surface code with and without syndrome degeneracy taken into account. Different panels correspond to (a,c) non-rotated and (b,d) rotated surface codes in the presence of (a,b) single-qubit and (c,d) two-qubit Pauli errors. Code stabilizers are chosen according to Fig. 6, such that only one of the sub-lattices is affected by a single two-qubit error event. Adding the degeneracy term has little, negative effect on the decoding fidelity when the non-rotated code (a) is used, while noticeably enhances it in the rotated code (b). When the code is subject to two-qubit errors, adding the degeneracy term has an opposite effect, as shown in (c,d). To generate the data in panels (a,b,c) the physical error rate is set to  $p = 0.1$  and in (d)  $p = 0.05$ .

## D Carbon footprint of numerical simulations

The carbon footprint associated with the numerical simulations in this paper are summarised below.

<b>Numerical simulations</b>	
Total Kernel Hours [h]	917323
Thermal Design Power Per Kernel [W]	5.75
Total Energy Consumption Simulations [kWh]	5275
Average Emission Of CO <sub>2</sub> in Germany [kg/kWh]	0.56
Were The Emissions Offset?	Yes
<b>Total CO<sub>2</sub>-Emission [kg]</b>	<b>2954</b>

Guidance on the reporting the carbon cost of scientific research can be found in Ref. [40].